Enhanced CO_2 Electrolysis with Metal-oxide Interface Structures①

XU Ze-Tong[a, b] XIE Kui[b②]

[a] (*College of Chemistry and Materials Science, Fujian Normal University, Fuzhou* 350007, *China*)

[b] (*CAS Key Laboratory of Design and Assembly of Functional Nanostructures, and Fujian Provincial Key Laboratory of Nanomaterials, Fujian Institute of Research on the Structure of Matter, Chinese Academy of Sciences, Fuzhou* 350002, *China*)

ABSTRACT The ever-decreasing fossil fuels and the increasing greenhouse effect have caused substantial concern. Solid oxide electrolyser cell (SOEC) with $La_{0.75}Sr_{0.25}Cr_{0.5}Mn_{0.5}O_{3-\delta}$ (LSCM) as a cathode was used for CO_2 electrolysis to CO. In this work, the metal-oxide interface was constructed on the LSCM framework by *in-situ* exsolution and impregnation, and the uniform distribution of metal nanoparticles on the LSCM framework was confirmed by spectroscopy techniques and electron microscopy techniques. The existence of three-phase boundary promoted the absorption and electrolysis of CO_2. $(La_{0.75}Sr_{0.25})_{0.9}(Cr_{0.5}Mn_{0.5})_{0.9}(Ni_{0.5}Cu_{0.5})_{0.1}O_{3-\delta}$ (LSCMNC) showed the best electrolytic CO_2 performance at 850 ℃ and exhibited excellent electrocatalytic activity after 100 hours of long-term testing and 8 redox cycles.

Keywords: solid oxide electrolyser cell, LSCM, metal nanoparticles, CO_2 electrolysis;

DOI: 10.14102/j.cnki.0254–5861.2011–2744

1 INTRODUCTION

The sustainable development of human society should to be realized by low-carbon economy model. The conversion and utilization of CO_2 could achieve a low-carbon economy model effectively[1, 2]. In recent years, the reduction of CO_2 by solid oxide electrolyser cell (SOEC), as an effective way to transform and utilize CO_2, can realize energy storage and green production[3]. During electrolysis of CO_2 by SOEC, a certain voltage is applied to the cathode at high temperature. CO_2 is cracked into CO and O^{2-}. O^{2-} is transported to the surface of the anode through the electrolyte and form O_2[4]. Nickel based cathodes materials for SOEC have excellent electrocatalytic properties. However, Ni-YSZ composite cathode needs to bring reducing gas to avoid the oxidation of cathode in the CO_2 electrolysis, and the poor redox stability and carbon deposition lead to a decrease of activity[5, 6]. LSCM has also been widely studied for its excellent redox stability[7-9]. Redox-stabilized LSCM can be operated without reducing gas compared with the Ni-YSZ composite cathode and exhibits stable catalysis performance as an anode material for SOFCs[10, 11]. However, the catalysis activity of LSCM is not satisfactory, so the exploration on LSCM is mainly focused on the improvement of its catalysis activity.

Oxide-loaded metal nanoparticles (NPs) are widely used in industry as heterogeneous catalysts[12-15]. According to Neagu et al., the metal NPs by *in-situ* exsolution loading on the anode substrate enhance the performance of solid oxide fuel cell (SOFC)[16]. Chen et al. reported that the introduction of active transition metal nanoparticles on the surface of perovskite electrode can improve the performance and stability of CO_2 electrolysis. The increase of catalytic activity is attributed to the strong metal/ceramic interactions[17]. In SOEC, the active site for CO_2 catalysis is located at the three-phase interface, and the construction of metal/oxide interface increases the specific surface area of the LSCM skeleton, thus greatly improving the adsorption and activation of CO_2[18].

The previous studies showed that the nano-sized metal

Received 20 January 2020; accepted 2 April 2020

① We acknowledge the funding support from the National Natural Science Foundation of China (91845202), Dalian National Laboratory for Clean Energy (DNL180404) and Strategic Priority Research Program of Chinese Academy of Sciences (XDB2000000)

② Corresponding author. Xie Kui, Professor. Tel: +86-591-63179173. E-mail: kxie@fjirsm.ac.cn

NPs obtained by reduction are conductive to the anchoring of CO_2 on the catalyst, and the transition state of activated CO_2 molecules is between CO_2 and carbonate. DFT theoretical calculations and experimental results show that the strong interaction between metal NPs and oxygen vacancies promote the cracking of CO_2. In our work, an active three-phase boundary is constructed on the cathode surface by *in-situ* exsolution and impregnation. The active nickel-LSCM and copper-LSCM electrodes were prepared by *in-situ* exsolution, and the nickel-copper-LSCM electrodes were prepared by *in-situ* exsolution and impregnation for direct CO_2 electrolysis. When using LSCMNC, the current density is 1.45 A·cm^{-2} at 2.0 V and 850 ℃. The LSCMNC electrode maintains prominent stability even after 100 hours of long-term testing and 8 redox cycles.

2 EXPERIMENTAL

2. 1 Material preparation

The $(La_{0.75}Sr_{0.25})_{0.9}(Cr_{0.5}Mn_{0.5})_{0.9}(Ni_{1-x}Cu_x)_{0.1}O_{3-\delta}$ (x = 0, 0.5 and 1) powders denoted as LSCM, LSCMN, LSCMC and LSCMNC, respectively were synthesized through a combustion method using certain ratios of La_2O_3, $SrCO_3$, $Cr(NO_3)_3 \cdot 9H_2O$, $C_4H_6MnO_4 \cdot 4H_2O$, NiO and CuO as well as glycine, then heated at 1200 ℃ for 5 h[8, 19]. $La_{0.75}Sr_{0.25}MnO_{3-\delta}$ (LSM) and $Ce_{0.8}Sm_{0.2}O_{2-\delta}$ (SDC) powders were synthesized by the glycine-nitrate combustion, then heated at 1200 ℃ for 5 h and 800 ℃ for 3 h in air, respectively[20]. The $La_{0.9}Sr_{0.1}Ga_{0.8}Mg_{0.2}O_{3-\delta}$ (LSGM) sample was composited using solid state reaction method with certain ratios of La_2O_3, $SrCO_3$, Ga_2O_3 and MgO mixed in acetone in a zirconia container with zirconia balls, followed by 1000 ℃ for 6 h and then pressed into a disc and sintered at 1500 ℃ for 6 h[21]. The LSCM-NC powders were obtained by impregnation method with certain molar ratios of LSCM, $Ni(NO_3)_2$ and $Cu(NO_3)_2$ solutions, and then heated at 800 ℃ for 1 h[22, 23]. All the chemical reagents (99.9%, AR) were purchased from Sinopec Chemical Reagent Co., Ltd. (China).

2. 2 Fabrication of cathode bars

The vertical bar with about 2.0 g LSCM, LSCMN, LSCMC, LSCMNC and LSCM-NC powders was pressed and sintered at 1400 ℃ for 10 h in air, separately[24].

2. 3 Single cell fabrication

The anode slurry, LSM-SDC (at weight ratio of 65:35) was synthesized by milling. Moreover, celluloses (20% of the total weight of anode slurry) and alpha-terpineol were added into slurry for porous materials. The cathode slurries (LSCM-SDC, LSCMN-SDC, LSCMC-SDC, LSCM-NC-SDC and LSCMNC-SDC) were fabricated by the same method.

The anode slurries were coated onto LSGM, and the cathode slurries were coated on the other side with an active area of 0.2 cm^2, then fired at 1100 ℃ for 3 h in air[10]. Ag paste was painted on both surfaces of LSGM, then Ag wires were stuck to both electrodes, which was followed by 550 ℃ for 0.5 h. The pure CO_2 was fed into the cathode side, while the anode was exposed to ambient air. Before test, for reduction and activation of cathode, the 5% H_2/Ar was fed for about 1 h and then pure H_2 for approximately 3 h.

3 RESULTS AND DISCUSSION

3. 1 Crystal structure

Fig. 1a and 1b show the XRD patterns of oxidized and reduced states $(La_{0.75}Sr_{0.25})_{0.9}(Cr_{0.5}Mn_{0.5})_{0.9}(Ni_{1-x}Cu_x)_{0.1}O_{3-\delta}$ (x = 0, 0.5 and 1), respectively. The crystal phase of oxidized $LaCrO_3$ was further confirmed by X-ray diffraction, which suggests that Ni and Cu can be successfully doped into LSCM. Peaks appearing in the reduced states can be indexed to Ni, Cu and $Ni_{1-x}Cu_x$ alloys (JCPDS: Ni: PDF#01-070-0989; Cu: PDF#00-001-1241; NiCu: PDF#03-065-9048) in Fig. 1b, respectively. The result implying that metals NPs Ni, Cu and NiCu can be successfully both *in-situ* exsolved and impregnated in LSCM powders. Also, no characteristic diffraction peaks of impurity phase are observed after reduction, suggesting the redox stability of cathode materials.

3. 2 Element valence

Fig. 2 shows the Ni 2*p* and Cu 2*p* XPS spectra of LSCMNC before and after reduction. Fig. 2a and Fig. 2c show the Ni 2*p* oxidation and reduction states, while Fig. 2b and Fig. 2d show Cu 2*p*. As shown in Fig. 2a and Fig. 2b, the Ni^{2+} $2p_{3/2}$, Ni^{2+} $2p_{1/2}$ and Cu^{2+} $2p_{3/2}$, Cu^{2+} $2p_{1/2}$ peaks of the oxidized LSCMNC are observed, respectively. Besides, it is observed that the peak of Ni^{2+} $2p_{3/2}$ is overlapped with La^{3+} 3*d* region. In the reduced sample, the coexistence of Ni ^{0}(Fig. 2c) and Cu ^{0}(Fig. 2d) in LSCMNC is observed, which is assigned to metals NiCu NPs[7, 8]. This result suggests that Ni^{2+} and Cu^{2+} in oxidized sample are reduced to Ni ^{0}and Cu ^{0}after treatment in the reducing stream.

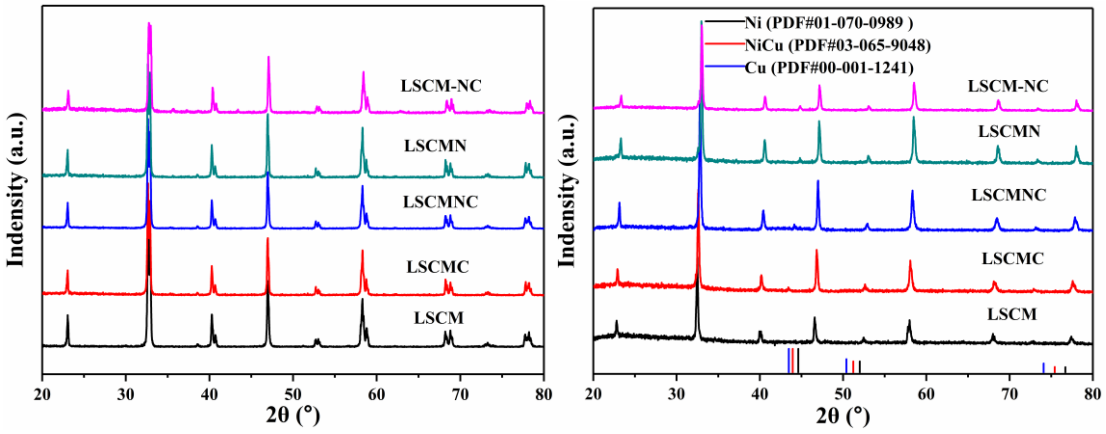

(a) **(b)**

Fig. 1. XRD of the cathode powders in oxidized and reduced states. (a) Oxidized samples, (b) Reduced samples

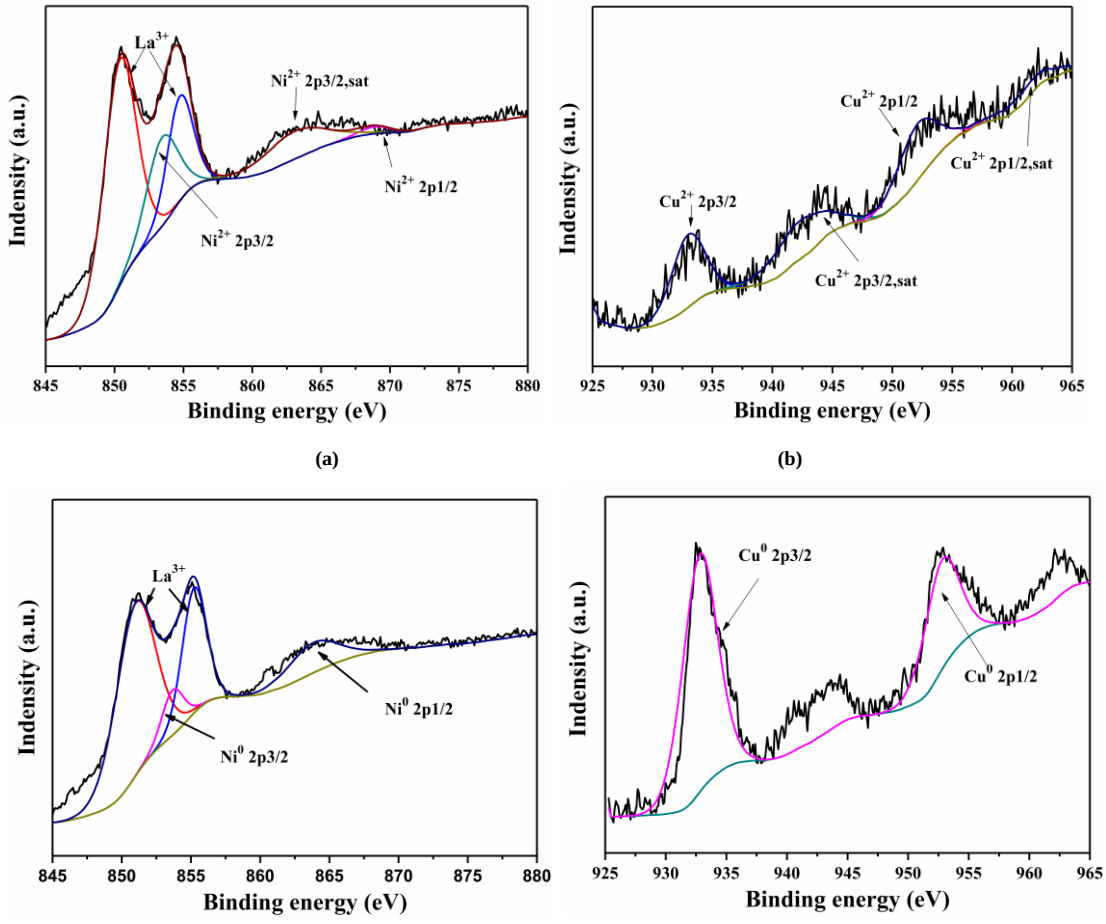

(a) **(b)**

(c) **(d)**

Fig. 2. Ni 2*p* (a) and Cu 2*p* (b) XPS spectra of oxidized LSCMNC sample, Ni 2*p* (c) and Cu 2*p* (d) XPS of reduced LSCMNC sample

3. 3 Microstructure

Fig. 3 displays the microstructure of different reduced cathode materials. The SEM images show that the Ni NPs (Fig. 3a) and Cu NPs (Fig. 3c) were well-distributed over LSCM perovskite scaffold with a narrow distribution in the average size of 45 to 65 nm. HRTEM (Fig. 3b) and SEM image (Fig. 3d) analyses found that the NiCu NPs in the reduced LSCMNC sample are anchored deeply over the LSCM hosts, while the SEM image in Fig. 3e shows the NiCu NPs

impregnated in the LSCM host. As shown Fig. 3b, the lattice fringes of NiCu NPs display interplanar spacings of 0.178 nm in the particle, which matches well with the X-ray diffraction. Also, SEM image in Fig. 3d shows the NiCu NPs distributed uniformly over a large area. SEM and TEM show the structure between metal NPs and LSCM skeleton. Moreover, the TEM analyses verify that Ni^{2+} and Cu^{2+} in oxidized LSCM–NC are reduced to NiCu alloy after high temperature reduction. This shows a good agreement between the observed and experimental results, and the anchoring of metal NP on the LSCM framework has a direct relationship with the inhibition of agglomeration, performance improvement and long-term stability[25]. Moreover, the EDS elemental maps (Fig. 4a to 4d) reveal that the compositional distributions of the three elements (O, Ni, and Cu) in the LSCMNC are uniform, while the distance between NPs and the anchorage between NPs and substrate maybe inhibits the agglomeration.

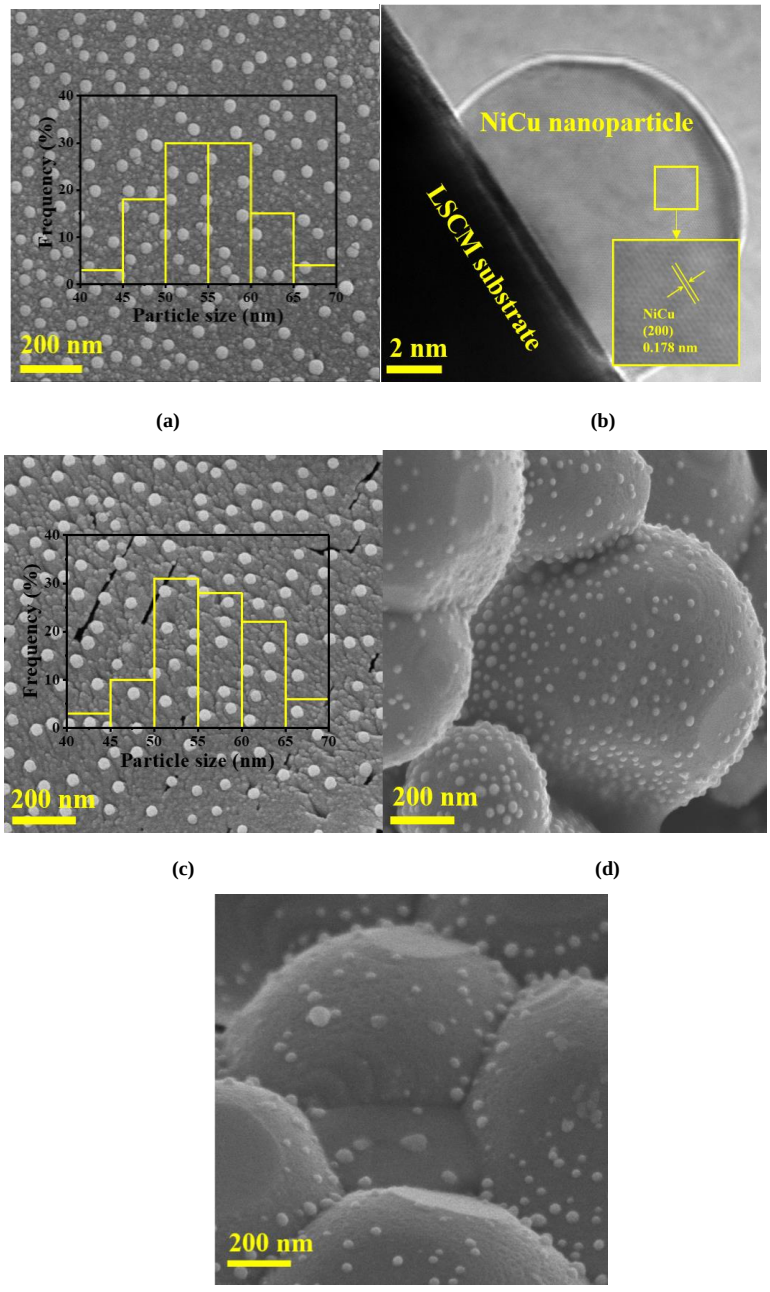

Fig. 3. (a) SEM images of the reduced LSCMN; (b) TEM image of the reduced LSCMNC; (c) SEM images of the reduced LSCMC; (d) SEM images of the reduced LSCMNC; (e) SEM images of the reduced LSCM-NC

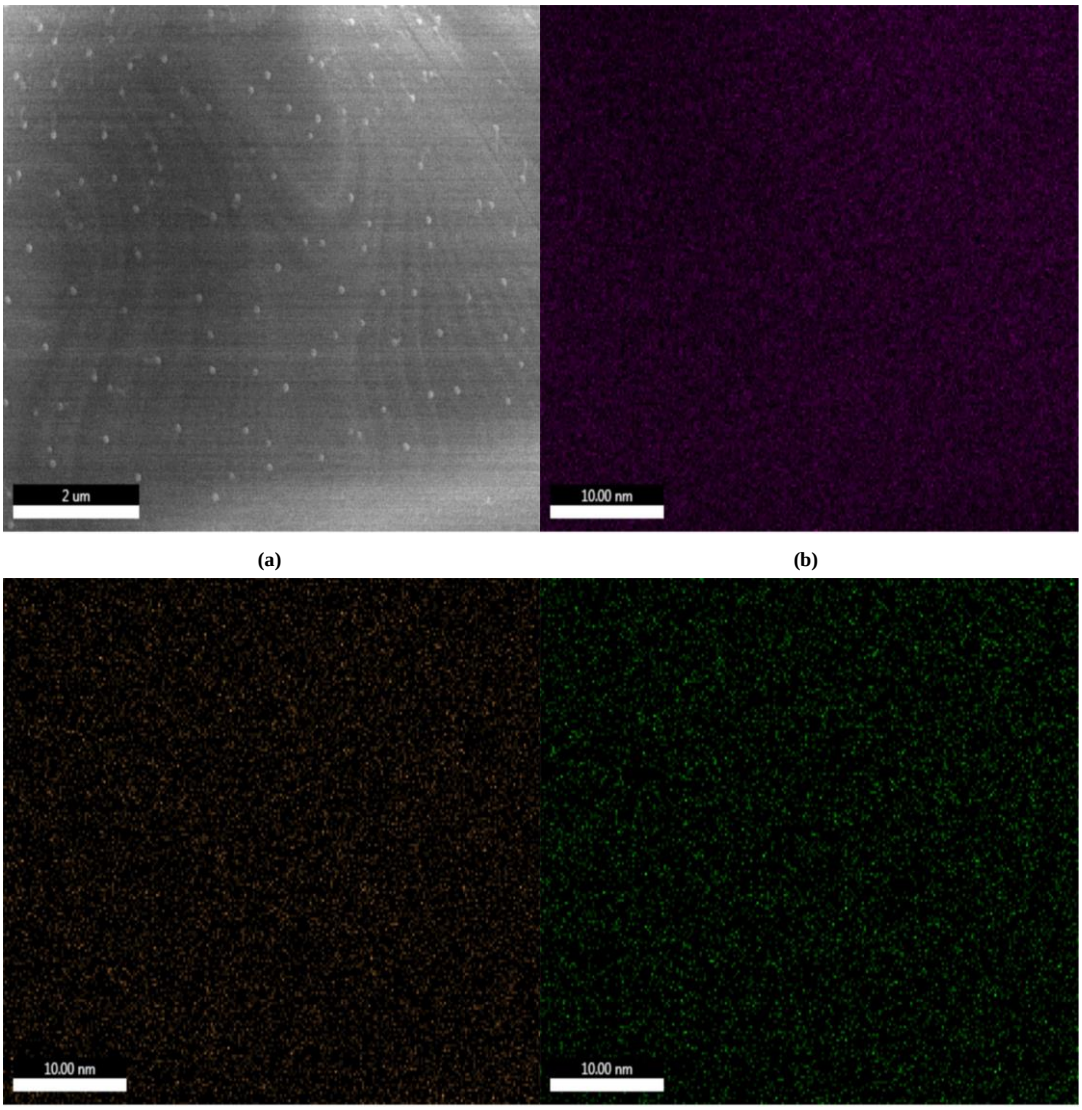

Fig. 4. SEM image (a) and (b) O, (c) Ni and (d) Cu EDS maps of reduced LSCMNC

3. 4 Oxygen nonstoichiometry and CO_2 adsorption

Thermogravimetric analysis (TGA) of reduced LSCM and LSCMNC in air is shown in Fig. 5a. Before test, LSCM and LSCMNC were placed and heated in 5% H_2/Ar for 20 h. The curve in the picture can be divided into three sections. Firstly, LSCM and LSCMNC keep the weight steady in 100～150 ℃, indicating that CO_2 and water vapor in the air do not affect the results of TGA. In the second stage, the reduced states LSCM and LSCMNC in 150～800 ℃ gain weight 0.07% and 1.52%, respectively, showing the samples were oxidized and the oxygen vacancy was occupied. In the last phase, the curves were stable once again in 800～1200 ℃, revealing that the sample has been fully oxidized and the weight remains stable. After reduction, the oxygen vacancy of LSCMNC reaches 21.6%, demonstrating that LSCMNC has good oxygen storage capacity and considerable active sites for adsorption and activation CO_2. FT-IR analysis was further carried out to verify chemical adsorption of CO_2 in the reduced cathode samples. As shown in Fig. 5b, after 20 h reduction of the cathode samples in 5% H_2/Ar, the intensities of the FT-IR peaks correspond to the oxygen functionalities, such as the molecular CO_2 stretching vibration peak at 2400～2300 cm^{-1}, and the carbonate ions (CO_3^{2-}) stretching peak at 1500～1400 cm^{-1}. All the cathode materials, meanwhile, show the absorption peak in the same place, indicating that the intermediate is the CO_2 and CO_3^{2-} species[26, 27]. Furthermore, the active metal NPs onto the LSCM skeleton are more advantageous to absorb and split CO_2.

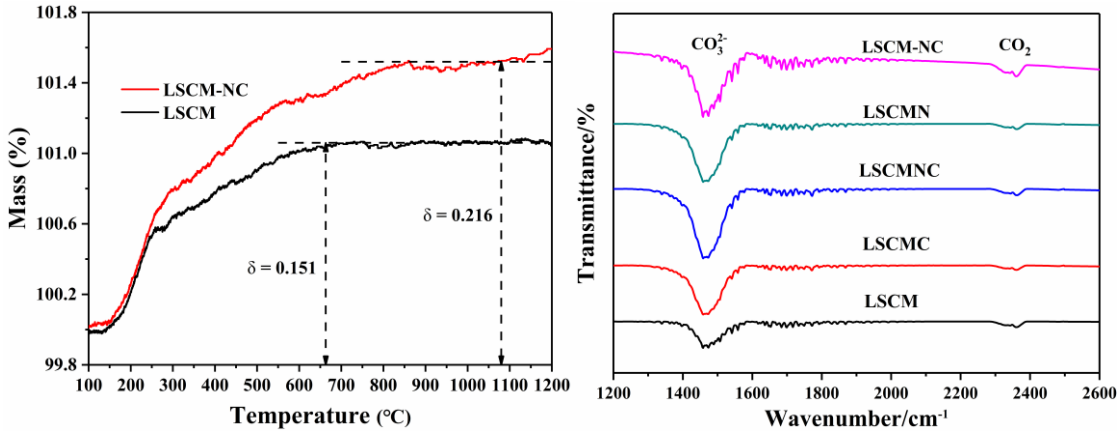

(a) (b)

Fig. 5. (a) TGA analysis of the reduced LSCM and LSCMNC from 100 to 1200 ℃; (b) FT-IR spectroscopy of CO_2 for cathode powders at 800 ℃

3. 5 Interface activity

Fig. 6 shows the normalized conductivity curve of the cathode materials at 800 ℃ with alternating changes in different oxygen partial pressures (pO_2: $10^{-18} \rightarrow 10^{-12}$ atm). Apparently, the electrical conductivity rebalancing time of LSCMNC is much shorter than that of LSCM, and the oxygen exchange coefficient (K_{ex}) increased about 5.7 times from 2.2 × 10^{-5} to 14.7 × 10^{-5} cm s^{-1}. We attribute the improvement of oxygen transfer ability to two aspects: one is that LSCMNC with high oxygen vacancy concentration is conducive to oxygen escape from the lattice; another is that NiCu alloy NPs embedded in LSCM skeleton will produce active metal-oxide interface with the LSCM scaffold, and the active site on the interface may promote the oxygen transmission.

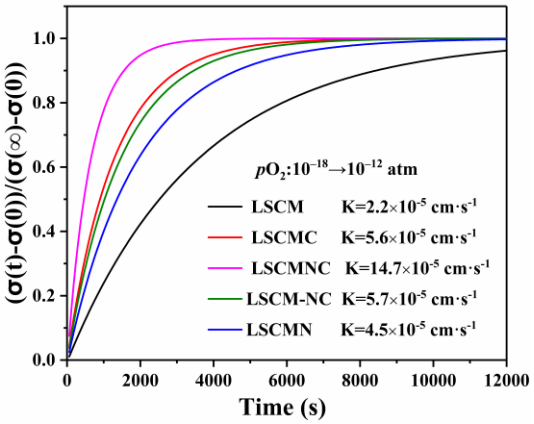

Fig. 6. Normalized conductivity profiles of reduced materials with an instantaneous gas change from 5% H_2/Ar to pure Ar at different temperature

3. 6 Carbon dioxide electrolysis

The SOEC single cell with different cathode materials was prepared for CO_2 electrolysis. Fig. 7a shows the current-voltage curve with the applied voltage from 1.0 to 2.0 V at 850 ℃. At 2.0 V, the current density with LSCMNC-SDC is 1.45 A cm^{-2}, which is a great improvement over 0.6 A cm^{-2} with LSCM-SDC. Under the same voltage, the current density of electrodes is shown below: LSCMNC-SDC (1.45 A cm^{-2}), followed by LSCM-NC-SDC (1.25 A cm^{-2}), LSMCN-SDC (1.15 A cm^{-2}), LSMMC-SDC (1.02 A cm^{-2}), and finally LSCM-SDC. In summary, LSCM-SDC electrodes with loading metal NPs are better than those without loading. LSCM-SDC with *in-situ* exsolution NiCu NPs is better than the impregnated one. Nickel-loading electrodes perform better than copper-loading. As a potential high-temperature oxygen-permeable material, some perovskite is able to adsorb and activate CO_2[28]. In addition, after loading metal NPs in bare LSCM, an active metal oxide

interface was formed, which may facilitate to adsorb and active CO_2 and then for CO_2 electrolysis[18]. At the same time, alloy NPs may be stronger than single metal NPs in upgrading CO_2 electrolysis[8]. LSCMNC-SDC has better performance than LSCM-NC-SDC, which can be explained by the preparation of electrode materials. The NPs in electrode materials obtained by *in-situ* exsolvation is more difficult to agglomerate on perovskite than that obtained by impregnation. In addition, the NPs distribution is uniform and size controllable. That is to say, the electrocatalytic performance of LSCMNC-SDC electrode is better than LSCM-NC-SDC due to the advantage of NPs loading mode and distribution. The short-term of CO_2 electrolysis at the given voltage is shown in Fig. 7b. As the applied voltage increases from 1.2 to 1.6 V, the current density is consistent with the variation tendency of the current-voltage curve, and there is unnoticeable attenuation of current density in short time, which shows that the electrode material has good stability.

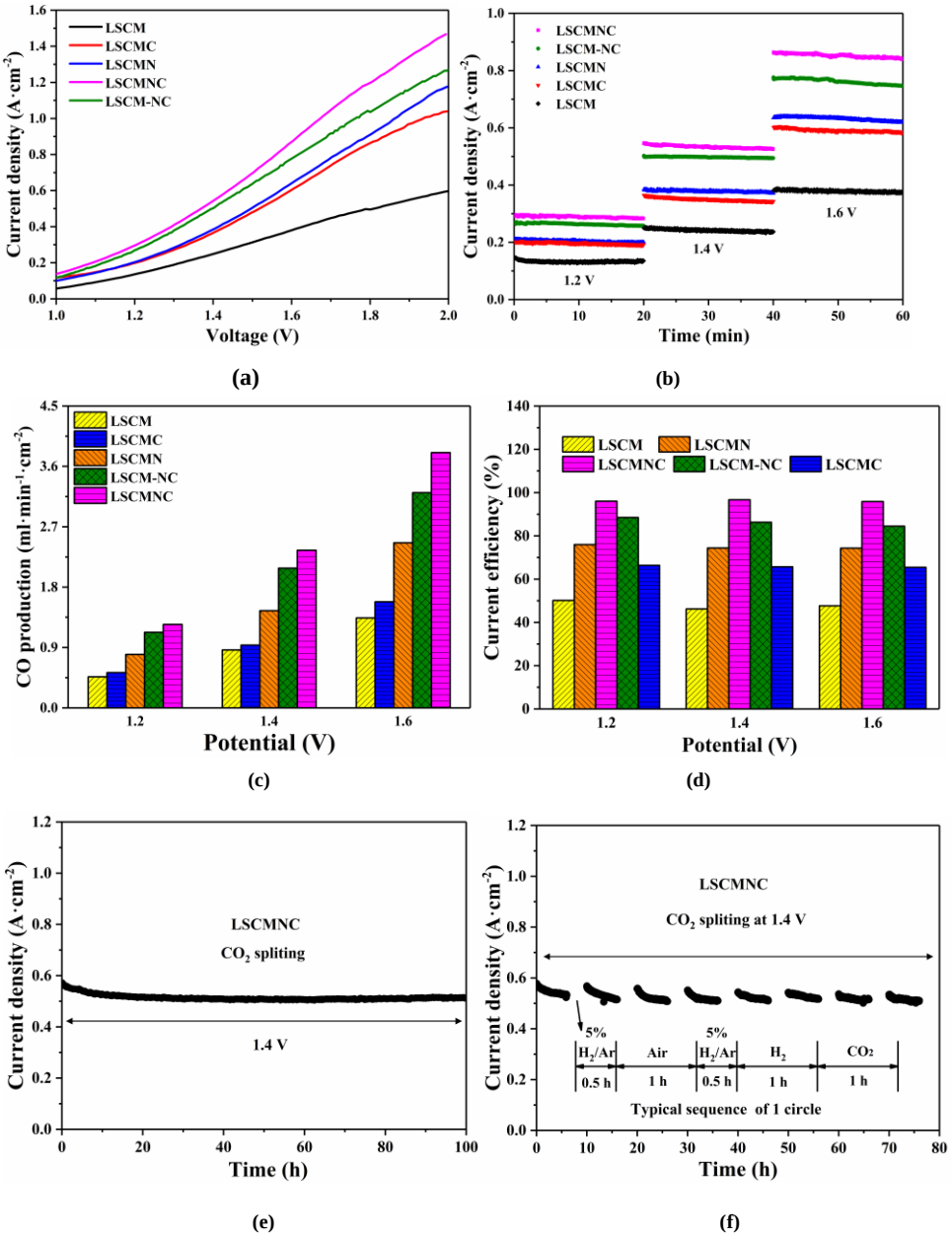

Fig. 7. Performances of CO_2 electrolysis for full cells with various cathode materials at 850 ℃. (a) I-V curves; (b) Short-term CO_2 electrolysis tests at different potentials; (c) CO production at different potentials; (d) Current efficiencies at different potentials; (e) Long-term CO_2 electrolysis test of the L SCMNC-SDC; (f) Redox-cycling performance of LSCMNC-SDC at 1.4 V

Fig. 7c and 7d show the CO yield and current efficiency of various electrodes, respectively. The CO yield was increasing with the increase of applied voltage from 1.2 to 1.6 V. It can be seen from graph that the yield of CO reaches 3.8 ml min^{-1} cm^{-2} when LSCMNC-SDC is used for CO_2 electrolysis, while the current efficiency is close to 100%. The yield has been improved greatly compared with unmodified LSCM-SDC and reported work[29]. As the applied voltage increases, the trend of CO yield is consistent with current efficiency and current density, indicating that the performance of electrode has been enhanced substantially by loading metal NPs by *in-situ* exsolution and impregnation[18, 24]. Besides, CO_2 electrolysis was performed at 1.4 V with LSCMNC-SDC in order to evaluate the durability and redox stability of the cathode. As shown in Fig. 7e, clearly, the long-term test shows the current density does not decrease significantly after 100 h high-temperature CO_2 electrolysis, suggesting that LSCMNC-SDC has outstanding durability for CO_2 electrolysis. Fig. 7f shows that LSCMNC-SDC keeps current density steady even after 8 redox-cycle alternating operations, which illustrates excellent oxidation-reduction stability of LSCMNC-SDC. The stability of LSCMNC-SDC might be attributed to the anchoring effect of the metal NPs-LSCM scaffold. The active metal Ni and Cu particles are anchored on the LSCM substrate, and the metal-oxide electrochemical active center is generated. The combination of active center and CO_2 reduce the activation energy, which is beneficial to the adsorption and activation of CO_2, and then enhances the CO_2 electrolytic performance. Compared with impregnation, the metal NPs obtained by *in-situ* exsolution is not easy to agglomerate and the combination of NPs and LSCM scaffold is more tight, so the number and activity of active sites remain stable[25].

Fig. 8a shows the XRD of LSCMNC-SDC electrode before and after CO_2 electrolysis. The upper line in the graph is the XRD before test, which shows that LSCMNC-SDC consists of two phases by the doped lanthanum chromate and cerium dioxide; while the lower line is XRD after test, indicating the NiCu alloy peak on XRD. Due to the partial vacancy of A site, the metal on B site was exsolved partially to form NiCu alloy in order to maintain the perovskite structure in reducing atmosphere. It can be seen from the picture that the peaks of LSCM can be corresponded before and after test, which proves that the main phase of LSCM has not changed. The overall shift of the peak may be caused by the instrument calibration or the difference in height between the two samples. Furthermore, the LSCM phase does not change in cathode after high temperature operation, which reflects the structural stability of electrode material. Fig. 8b shows the cross-sectional SEM image of the cell after 100 h for electrolysis CO_2. Macroscopically, the cell is divided into two parts. The lower part is a dense LSGM electrolyte and the upper part is a porous LSCMNiCu-SDC electrode. It is in favor of gas flow. Microcosmically, the NiCu alloy NPs were distributed on the LSCM skeleton evenly without agglomeration. Overall, the LSCMNC shows outstanding structural stability.

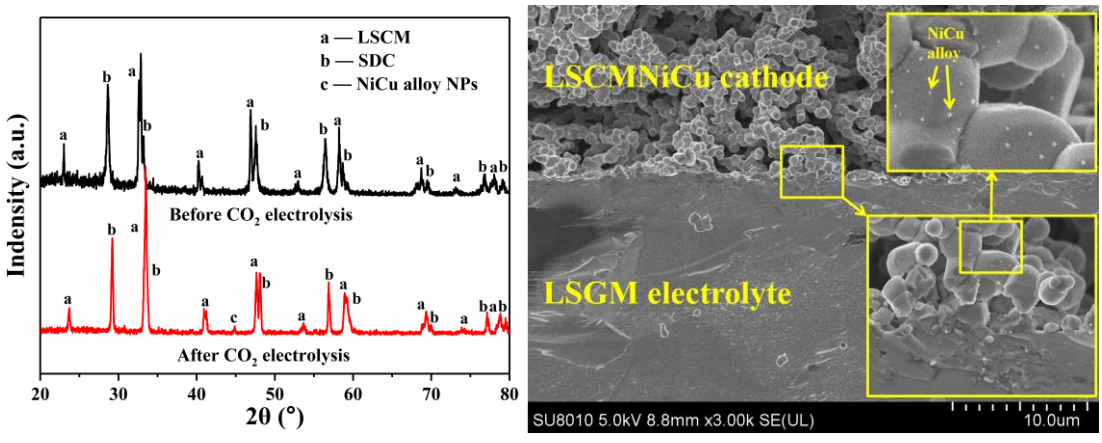

(a) **(b)**

Fig. 8. (a) XRD of LSCMNC-SDC before and after CO_2 electrolysis. (b) Cross-sectional SEM image for full cells with Ag/LSCMNiCu-SDC/LSGM/LSM-SDC/Ag

In-situ AC impedance spectroscopy is often used to explain the reasons for the improved performance of SOEC. Fig. 9 shows the *in-situ* AC impedance spectroscopy in 800 ℃ with different electrodes at specific voltages. It can be seen from Fig. 9a to Fig. 9e that the polarization resistance (Rp) which was calculated using review[30] with the increase of applied voltage decreases significantly, while the series resistances (Rs) of cathode remain stable ～0.4 Ω·cm^2. Fig. 8e shows the polarization resistance as small as 0.32 Ω·cm^2 at 1.6 V with LSCMNC-SDC. This result shows that *in-situ* exsolution and impregnation of metal NPs on the LSCM framework are able to improve the catalytic activity and reduce the polarization resistance for SOEC effectively. Among them, the *in-situ* exsolution is much better than impregnation on the loading method.

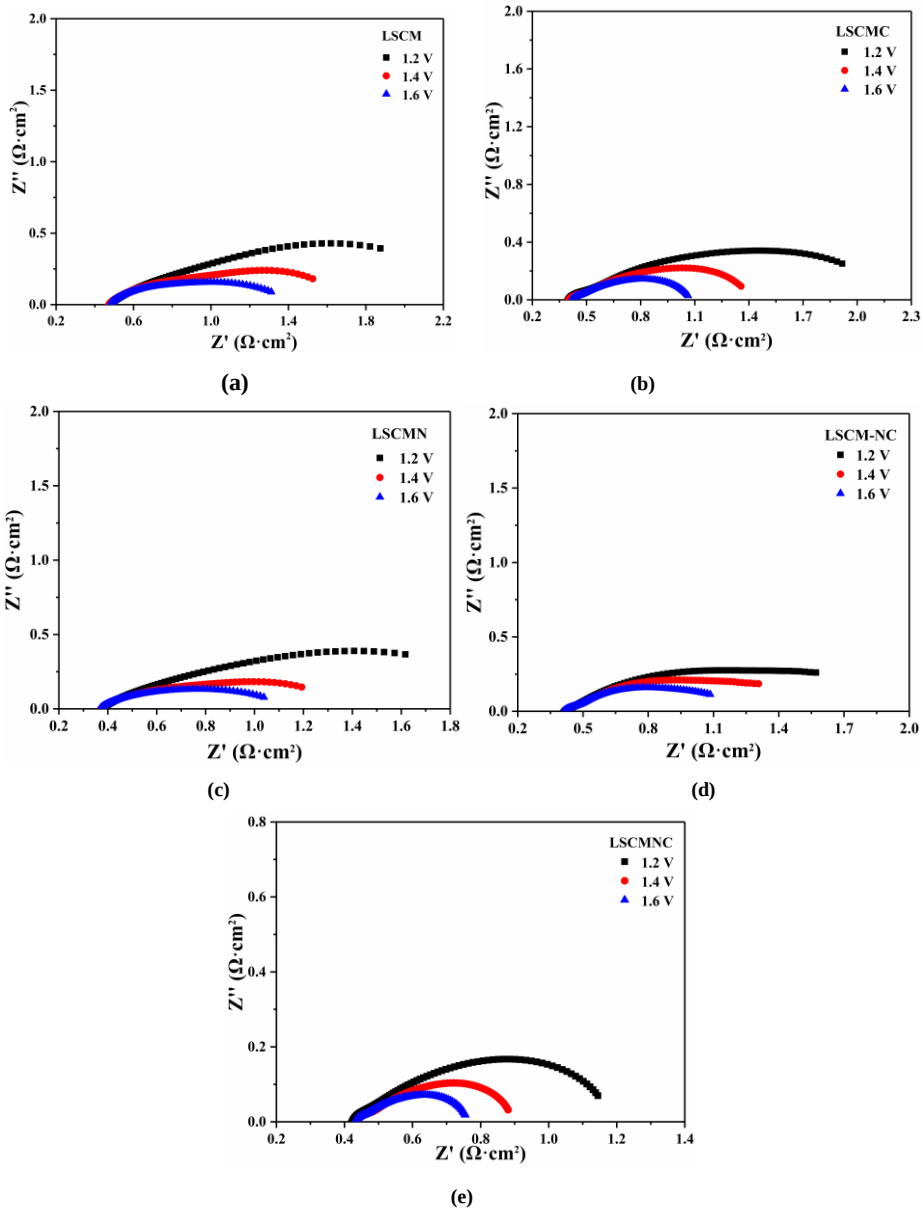

Fig. 9. AC impedance spectra of the full cells with a series of cathode materials for pure CO_2 electrolysis at 800 ℃

4 CONCLUSION

In general, the metal NPs are supported on the LSCM skeleton by *in-situ* exsolution and impregnation, which enhances the electrode activity of LSCM and promotes the electrolytic performance, and the way by *in-situ* exsolution is much better than impregnation. In this work, the excellent chemisorption and activation of CO_2 are attributed to the active three-phase boundary. Metal NPs (Ni, Cu, and NiCu alloy) are distributed on the LSCM skeleton uniformly. In

this way an electrocatalytic active three-phase boundary was architected. At 850 ℃ and 2.0 V, the maximum current density is 1.45 A cm^2 when LSCMNC-SDC is used for CO_2 electrolysis. Also, the LSCMNC-SDC cathode exhibits excellent long-term stability after 100 h in high temperature operation and 8 redox cycles.

REFERENCES

(1) Ampelli, C.; Perathoner, S.; Centi, G. CO_2 utilization: an enabling element to move to a resourceand energy-efficient chemical and fuel production. *Phil. Trans. R. Soc. A* **2015**, 373, 20140177–35.

(2) Tahir, M.; Amin, N. S. Recycling of carbon dioxide to renewable fuels by photo catalysis: prospects and challenges. *Renew. Sust. Energ. Rev.* **2013**, 25, 560–579.

(3) Duan, C. C.; Kee, R.; Zhu, H. Y.; Sullivan, N.; Zhu, L. Z.; Bian, L. Z.; Jennings, D.; O'Hayre, R. Highly efficient reversible protonic ceramic electrochemical cells for power generation and fuel production. *Nat. Energy* **2019**, 4, 230–240.

(4) Bidrawn, F.; Kim, G.; Corre, G.; Irvine, J. T. S.; Vohs, J. M.; Gorte, R. J. Efficient reduction of CO_2 in a solid oxide electrolyzer. *Electrochem. Solid-State Lett*. **2008**, 11, B167–B170.

(5) Singh, V.; Muroyama, H.; Matsui, T.; Hashigami, S.; Inagaki, T.; Eguchi, K. Feasibility of alternative electrode materials for high temperature CO_2 reduction on solid oxide electrolysis cell. *J. Power Sources* **2015**, 293, 642–648.

(6) Laguna-Bercero, M. A.; Skinner, S. J.; Kilner, J. A. Performance of solid oxide electrolysis cells based on scandia stabilised zirconia. *J. Power Sources* **2009**, 192, 126–131.

(7) Zhu, C. L.; Hou, L. X.; Li, S. S.; Gan, L. Z.; Xie, K. Efficient carbon dioxide electrolysis with metal nanoparticles loaded $La_{0.75}Sr_{0.25}Cr_{0.5}Mn_{0.5}O_{3-\delta}$ cathodes. *J. Power Sources* **2017**, 363, 177–184.

(8) Lu, J. H.; Zhu, C. L.; Pan, C. C.; Lin, W. L.; Lemmon, J. P.; Chen, F. L.; Li, C. S.; Xie, K. Highly efficient electrochemical reforming of CH_4/CO_2 in a solid oxide electrolyser. *Sci. Adv.* **2018**, 4, eaar5100–9.

(9) Tao, S. W.; Irvine, J. T. S.; Plint, S. M. Methane oxidation at redox stable fuel cell electrode $La_{0.75}Sr_{0.25}Cr_{0.5}Mn_{0.5}O_{3-\delta}$. *J. Phys. Chem. B* **2006**, 110, 21771–21776.

(10) Xu, S. S.; Li, S. S.; Yao, W. T.; Dong, D. H.; Xie, K. Direct electrolysis of CO_2 using an oxygen-ion conducting solid oxide electrolyzer based on $La_{0.75}Sr_{0.25}Cr_{0.5}Mn_{0.5}O_{3-\delta}$ electrode. *J. Power Sources* **2013**, 230, 115–121.

(11) Wang, W. Y.; Zhu, C. L.; Xie, K.; Gan, L. Z. High performance, coking-resistant and sulfur-tolerant anode for solid oxide fuel cell. *J. Power Sources* **2018**, 406, 1–6.

(12) Sun, Z. Y.; Jin, L.; He, S.; Zhao, Y. F.; Wei, M.; Evans, D. G.; Duan, X. A structured catalyst based on cobalt phthalocyanine/calcined Mg–Al hydrotalcite film for the oxidation of mercaptan. *Green Chem.* **2012**, 14, 1909–1916.

(13) Feng, J. T.; He, Y. F.; Liu, Y. N.; Du, Y.; Li, D. Q. Supported catalysts based on layered double hydroxides for catalytic oxidation and hydrogenation: general functionality and promising application prospects. *Chem. Soc. Rev*. **2015**, 44, 5291–5319.

(14) Sun, Z. Y.; Jin, L.; Zhao, Y. F.; He, S.; Li, S. D.; Wei, M.; Wang, L. R. A structured catalyst toward mercaptan sweetening with largely enhanced synergistic effect. *Ind. Eng. Chem. Res*. **2014**, 53, 4595–4603.

(15) Claure, M. T.; Chai, S. H.; Dai, S.; Unocic, K. A.; Alamgir, F. M.; Agrawal, P. K.; Jones, C. W. Tuning of higher alcohol selectivity and productivity in CO hydrogenation reactions over K/MoS_2 domains supported on mesoporous activated carbon and mixed MgAl oxide. *J. Catal.* **2015**, 324, 88–97.

(16) Neagu, D.; Oh, T. S.; Miller, D. N.; Menard, H.; Bukhari, S. M.; Gamble, S. R.; Gorte, R. J.; Vohs, J. M.; Irvine, J. T. S. Nano-socketed nickel particles with enhanced coking resistance grown in situ by redox exsolution. *Nat. Commun*. **2015**, 6, 8120–8.

(17) Li, Y. H.; Hu, B. B.; Xia, C. R.; Xu, W. Q.; Lemmon, J. P.; Chen, F. L. A novel fuel electrode enabling direct CO_2 electrolysis with excellent and stable cell performance. *J. Mater. Chem. A* **2017**, 5, 20833–20842.

(18) Wang, W. Y.; Gan, L. Z.; Lemmon, J. P.; Chen, F. L.; Irvine, J. T. S.; Xie, K. Enhanced carbon dioxide electrolysis at redox manipulated interfaces. *Nat. Commun*. **2019**, 10, 1550–10.

(19) Shi, L.; Zeng, C. Y.; Jin, Y. Z.; Wang, T. J.; Tsubaki, N. A sol-gel auto-combustion method to prepare Cu/ZnO catalysts for low-temperature methanol synthesis. *Catal. Sci. Technol*. **2012**, 2, 2569–2577.

(20) Jung, G. B.; Huang, T. J. Sintering temperature, microstructure and resistivity of polycrystalline $Sm_{0.2}Ce_{0.8}O_{1.9}$ as SOFC's electrolyte. *J. Mater. Sci*. **2003**, 38, 2461–2468.

(21) Ishihara, T.; Honda, M.; Shibayama, T.; Furutani, H.; Takita, Y. An intermediate temperature solid oxide fuel cell utilizing superior oxide ion conducting electrolyte, doubly doped $LaGaO_3$ perovskite. *Ionics* **1998**, 4, 395–402.

(22) Xu, S. S.; Chen, S. G.; Li, M.; Xie, K.; Wang, Y.; Wu, Y. C. Composite cathode based on Fe-loaded LSCM for steam electrolysis in an oxide-ion-conducting solid oxide electrolyser. *J. Power Sources* **2013**, 239, 332–340.

(23) Li, Y. X.; Gan, Y.; Wang, Y.; Xie, K.; Wu, Y. C. Composite cathode based on Ni-loaded $La_{0.75}Sr_{0.25}Cr_{0.5}Mn_{0.5}O_{3-\delta}$ for direct steam electrolysis in an oxide-ion-conducting solid oxide electrolyzer. *Int. J. Hydrogen Energy* **2013**, 38, 10196–10207.

(24) Ye, L. T.; Zhang, M. Y.; Huang, P.; Guo, G. C.; Hong, M. C.; Li, C. S.; Irvine, J. T. S.; Xie, K. Enhancing CO_2 electrolysis through synergistic control of non-stoichiometry and doping to tune cathode surface structures. *Nat. Commun*. **2017**, 8, 14785–10.

(25) Irvine, J. T. S.; Neagu, D.; Verbraeken, M. C.; Chatzichristodoulou, C.; Graves, C.; Mogensen, M. B. Evolution of the electrochemical interface in high temperature fuel cells and electrolysers. *Nat. Energy* **2016**, 1, 15014–26.

(26) Garza, A. J.; Bell, A. T.; Head-Gordon, M. On the mechanism of CO_2 reduction at copper surfaces: pathways to C2 products. *ACS Catal*. **2018**, 8, 1490–1499.

(27) Su, W. G.; Zhang, J.; Feng, Z. C.; Chen, T.; Ying, P. L.; Li, C. Surface phases of TiO_2 nanoparticles studied by UV Raman spectroscopy and FT-IR spectroscopy. *J. Phys. Chem. C* **2008**, 112, 7710–7716.

(28) Daza, Y. A.; Kent, R. A.; Yung, M. M.; Kuhn, J. N. Carbon dioxide conversion by reverse water-gas shift chemical looping on perovskite-type oxides. *Ind. Eng. Chem. Res*. **2014**, 53, 5828–5837.

(29) Zhang, X. Z.; Ye, L. T.; Hu, J. P.; Li, J.; Jiang, W. H.; Tseng, C. J.; Xie, K. Perovskite LSCM impregnated with vanadium pentoxide for high temperature carbon dioxide electrolysis. *Electrochim. Acta* **2016**, 212, 32–40.

(30) Gan, L. Z.; Ye, L. T.; Ruan, C.; Chen, S. G.; Xie, K. Redox-reversible iron orthovanadate cathode for solid oxide steam electrolyzer. *Adv. Sci*. **2016**, 3, 1500186–7.